# Establishing an integrated workflow identifying and linking surface and subsurface lineaments for mineral exploration under cover: Example from the Gawler Craton, South Australia

Ulrich Kelka[1], Cericia Martinez[1], Carmen Krapf[2], Stefan Westerlund[1], Ignacio Gonzalez-Alvarez[3,4], Mark Pawley[2], and Clive Foss[1]

[1]CSIRO - Deep Earth Imaging Future Science Platform, Australia
[2]Geological Survey of South Australia, Department for Energy and Mining, Australia
[3]CSIRO - Mineral Resources, Discovery Program, Australia
[4]University of Western Australia, Centre for Exploration Targeting, Perth, Australia

**Correspondence:** Ulrich Kelka(uli.kelka@csiro.au)

**Abstract.** Mineral exploration in areas comprising thick and complex cover represents an intrinsic challenge. Cost and time efficient methods that help to narrow down exploration areas are therefore of particular interest to the Australian mining industry and for mineral exploration world wide. Based on a case study around the Tarcoola gold mine in the regolith dominated South Australian central Gawler Craton we suggest an exploration targeting workflow based on the joint analysis of surface and subsurface lineaments. The datasets utilized in this study are a digital elevation model and radiometrics that represent surface signals and total magnetic intensity and gravity attributed to subsurface signals. We compare automatically and manually mapped lineament sets derived from remotely sensed data. In order to establish an integrated concept for exploration through cover based on the best suited lineament data, we will point out the most striking differences between the automatically and manually detected lineaments and compare the datasets that represent surficial in contrast to subsurface structures. ~~After determining which mapping technique is best suited for preliminary exploration in regions comprising thick cover, we will show how merging~~ We further show how lineaments derived from surface and subsurface ~~lineament data may prove useful for mapping prospective areas~~ datasets can be combined to obtain targeting maps that help to narrow down areas for mineral exploration. We propose that target areas are represented by high lineament densities that are adjacent to regions comprising high density of intersections.

*Copyright statement.* TEXT

## 1  Introduction

The Gawler Craton (Figure 1a) is one of the three largest Archean to Proterozic Cratons within the Australian Continent (Figure 1b) and the major crustal province in South Australia (Hand et al., 2007). Australian Cratons are rich in mineralization (e.g., Pilbara and Yilgarn Craton (Witt et al., 1998)) and the Gawler Craton hosts significant economic mineralization such as

20   Olympic Dam, Challenger, Prominent Hill, and Tarcoola. The discovery of new deposits is particularly challenging in this part of Australia due to limited surface outcrops, variable thickness and complexity of the cover, with few surface features that can be used as direct proxies for mineral exploration.

To narrow down potential areas for exploration, and to enhance the general understanding of the geology, the Geological Survey of South Australia (GSSA) has recently acquired high-resolution magnetic, radiometric, and digital elevation data

25   across the Gawler Craton via the Gawler Craton Airborne Survey (GCAS) (Katona et al., 2019). Here we utilize these and previously acquired gravity datasets for the extraction of lineaments from surface (digital elevation model (DEM) and radiometrics) and subsurface (magnetics and gravity) datasets. Lineaments are linear features which can reflect geological structures and the extraction of such features can be important for mineral exploration, as well as for the investigation of fault activity (neotectonic) and water resource analysis (Vassilas et al., 2002). In images, photos, or maps, lineaments are represented by

30   straight or slightly curved lines, linear patterns or an alignment of discontinuity patterns (Wang, 1993). A relationship between lineaments and mineralization has been suggested for a long time and proven a useful tool for mineral exploration (O'Driscoll, 1986). We can distinguish between surface lineaments that are obtained from surface data and geophysical lineaments that are derived from processed geophysical data whereas it is widely assumed that surface lineaments represent structural features which, in the simplest model, are related to dip-slip or strike-slip faults (Florinsky, 2016). This assumes that a considerable

35   displacement is associated with faulting in the subsurface that leads to a detectable pattern on the surface (Boucher, 1997). In contrast, geophysical lineaments represent major subsurface boundaries (e.g. Hall, 1986; Langenheim and Hildenbrand, 1997) that are not necessarily associated with faults but rather with lithological or petrophysical contrasts. It is important to note that datasets such as lidar, digital elevation models, or radiometrics data represent only the change in surface properties such as elevation or surface geology.

40   We choose the As a case study for mineral exploration, we choose an area in the South Australian central Gawler craton around the Tarcoola mine, an Au-deposit mined for over 125 years (Daly et al., 1990). As the structural structurally controlled mineralization often localizes around discontinuity intersections (Wilson et al., 2018), this area represents a perfect study area for investigating the potential of surface and subsurface lineaments as a potential exploration targeting tool. The thick and complex cover (up to 500m500 m) overlying the basement units makes it particularly challenging to identify target areas and

45   a cost efficient approach to exploration targeting is desirable in such a region. A great challenge is that surface impressions of basement hosted displacement structures can be offset compared to the location of the large-scale discontinuity in the basement. Furthermore, cross-strike features are likely associated with small scale shears that will not be traceable in potential field data that images basement structures. A reliable interpretation of surface and subsurface lineament sets is particularity challenging in an old crustal block such as the Gawler Craton and we consider the work presented here as an first attempt to unify a

50   lineament-based workflow for exploration targeting in such an environment.

In this study, we use the above-mentioned new GCAS datasets to identify surface and subsurface lineament features and design a workflow to automatically extract and analyse these features. We assume that elevation and radiometric data relates to surficial features, while gravity and magnetics data represent structuresbelow the cover. This study is part of a broader effort to

~~geologically link basement architecture with surface linear features, landforms, and landscape variability in the central Gawler~~

55 ~~Craton (González-Álvarez et al., 2020).~~

~~Towards that end, we further explore the use of targeting maps based on surface and subsurface lineaments~~ Lineaments will be extracted manually and automatically. The automatic segmentation is either performed using PCI Geomatics LINE algorithm or an edge detection algorithm ("worms"). The latter is only applied to the geophysical lineaments obtained from gravity and magnetic data. We will show the variability in terms of lineament length and principal orientations between the different

60 extraction methods (1) and will demonstrate how lineament data can be used for exploration targeting (2). Targeting maps derived from lineament analysis are often based on the density of lineaments per unit area. Density maps combining subsurface lineaments (potential field data) and surface lineaments (digital elevation model and satellite imagery) were proposed as an exploration tool for groundwater (Epuh et al., 2020) and for mineral exploration (Mohammadpour et al., 2020). Lineament intersections were also used previously for the analysis of groundwater (Ilugbo and Adebiyi, 2017) and locations of intersecting

65 structural elements were suggested to represent favourable target areas for mineral exploration ~~(~~Sheikhrahimi et al., 2019; González-Álvarez et al., 2019; Krapf and Gonzalez-Alvarez, 2018; González-Álvarez et al., 2020). In hydrocarbon exploration cross-strike discontinuities were suggested as an exploration tool for natural gas (Wheeler, 1980).

~~We apply edge enhancement filtering to digital elevation data and perform automatic and manual lineament extraction on all datasets to compare both approaches and results. We discuss the advantages and shortcomings of different edge detection filters~~

70 ~~applied to the subsurface and surface datasets and present a workflow (~~In this contribution, we will show how lineament density and intersection density maps can be combined for identifying target areas for more detailed exploration. The underlying workflow is shown schematically in Figure 1~~a) to help with the identification of linear features~~~~that could be linked to main~~ ~~basement geological features~~c. This study is part of a broader effort to link basement architecture with surface linear features, landforms, and landscape variability in the central Gawler Craton (González-Álvarez et al., 2020).

75 ## 2 Geological Overview

The Gawler Craton is the oldest and largest geological province in South Australia and represents one of the three ~~mayor~~ major Australian Cratons (Figure 1~~e~~b). The region ~~is host to~~ hosts several economic iron oxide copper gold ore deposits (IOGC) ~~of~~ ~~which Olympic Dam is world class~~ including the world class Olympic Dam (Figure 1~~b). Part of this style of mineralisation~~ ~~is the Olympic IOGC province , which~~ a). The Olympic IOCG province forms a 100 to ~~200km wide roughly~~ 200 km wide

80 north-south trending belt at the eastern margin of the Gawler Craton (Skirrow et al., 2007). The largest known mineral occurrence in the area investigated is the Tarcoola Mine~~that~~, which hosts disseminated or veinlet-type Au-mineralization mainly in brittle to brittle-ductile faults and shears (Hand et al., 2007). The age of the Tarcoola Au-mineralization is considered to be 1564Ma (Bockmann et al., 2019) and the timing of the ore-formation at the Tunkilla project ($\approx$ 70km S/SE of Tarcoola) has been constrained at 1590-1570Ma (Budd and Fraser, 2004). Ongoing exploration in the central Gawler Craton targets

85 Au, Cu-Au, Pb-Zn, Fe, and Ni in the crystalline basement (Sheard et al., 2008). The expected commodities within the investigated region are mainly Au and Fe and are likely located in proximity to crustal scale structures that provided conduits

for the upwelling of deep crustal fluids. Such large scale reactivated tectonic features often form major crustal boundaries that are detectable with potential-field methods (Motta et al., 2019). It was shown that Archean gold mineralizations are often associated with such crustal-scale shear zones (Eisenlohr et al., 1989; Budd and Fraser, 2004). If a surface expression of such structures exists, this may be indicative that the crustal structures remained active for a long time resulting in a high amount of deformation or strong lithological contrasts. In the framework of the central Gawler mineral-systems, the vicinity of such structures indicates potential exploration targets.

Three major orogenic events, corresponding to crustal deformation and tectono-thermal alterations, are recorded by the crystalline basement of the Gawler Craton: the Sleaford Orogeny (Paleoproterozoic, 2440 Ma), the Kimban Orogeny (Paleoproterozoic, 1845–1700 Ma), and the Kararan Orogeny (Mesoproterozoic, 1650–1540 Ma) (Ferris et al., 2002; Swain et al., 2005; Reid et al., 2014; Kositcin, 2010). Three major mineral systems are related to these three deformation-magmatic events and the Tarcoola mineral field is attributed only to the Kararan system ($\approx$ 1570 Ma) (Gum, 2019). As outlined by Hand et al. (2007), the exact timing and spatial distribution of the tectonostratigraphic sequences within the Gawler Craton remain a controversy and reworking of existing mineralization during reactivation of existing crustal-scale fluid conduits has to be considered (Gum, 2019). The last large-scale deformation in the Gawler Craton was the reactivation of shear zones between 1470 and 1450 Ma (Hand et al., 2007). After this time, only minor near-surface movements are recorded (Sheard et al., 2008). Given the mineralization is linked to the youngest orogeny in the area (Kararan Orogon) and only minor tectonic activity is evident in the area after this event, we can assume that links between surficial and subsurface features point to areas of high defomation and/or neotectonics activity.

The bulk of the Paleo- to Mesoproterozoic rocks of the Gawler Craton enclose an Archean Core in the central Gawler Craton with the oldest units being of Late Archean age (Reid et al., 2014). Internally, the Gawler Craton is subdivided into different domains based on contrasts in magnetic, gravity, lithological, structural, geochronological, isotopic, and geochemical characteristics (Ferris et al., 2002; Fairclough et al., 2003; Kositcin, 2010). The different rock units are often separated by crustal-scale shear zones that often coincide with the boundaries of the individual blocks. The region around Tarcoola includes four major provinces of the central Galwer Cratons: the Christie, Wilgena, and Nuyts subdomains, and the Harris Greenstone belt (Figure 2a).

## 2.1 Basement and cover sequence

The key geologic features that we seek to explore are structural and lithology discontinuities in the basement along with if and how they may relate to today's landscape and current topographic relief. In the following we briefly describe the dominant lithologies in the study area from the oldest to youngest unit and highlight the expected variability in aeromagnetic and gravity data.

The interpreted Precambrian basement geology of the Harris Greenstone Belt comprises east-northeast-trending linear magnetic highs that often correlate with broad gravity signatures and are flanked by ovoid to elongated magnetic lows and
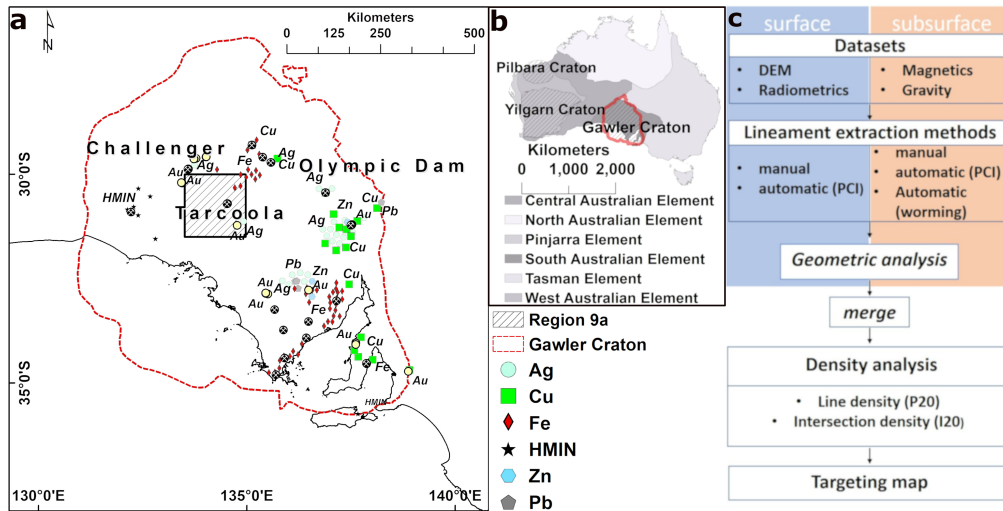
**Figure 1. a** ~~Large~~ Economic mineral occurrences in the Gawler Craton. The ~~economic~~ mineral commodities include Cu, Au, Fe, Ag, Pb, Zn, Co, Ni, Cr, Mn, Ti, V, PGE, Mo, W, Sn, and REE. **b** Overview map of the Australian continent showing the major crustal blocks and the locations of mineral rich Archean to Proterozoic tectonic provinces. The Gawler Craton spans across nearly the entire South Australian Crustal element. **c** Outline of the workflow applied in this study to obtain targeting maps from surface and subsurface datasets.

120     highs (Hoatson et al., 2002). Rocks of the Harris Greenstone Belt are found along the Flinke and Yerda Shear Zones and at the eastern margin in the central part of Figure 2b.

    Most rocks in the region are of igneous origin with only minor portions of metasediments. Rocks of the Hiltaba Suite (see of legend Figure 2) are prominent within the area of interest ~~and include~~ along with large plutons. The northeastern part of the study area was affected by the ~~predominantly northwest-trending~~ Gairdner Dyke Swarm at 827 Ma that comprises
125  predominantly northwest-trending dykes (Huang et al., 2015, and references therein). The youngest structure in the region is the Mulgathing Trough in the north western that has an inferred Permian age.

    ~~Most rocks in the region are of igneous origin with only minor portions of metasediments.~~ The magnetic signatures could help to distinguish between different rock types as suggested by Hoatson et al. (2002) who showed that Archean granitic gneisses and granites are often irregular or elongated bodies with low amplitude magnetic signatures, whereas Proterozoic
130  granites comprise both zoned and massive ovoid plutons of low and high magnetization. For the Hitaba Suite, Schmidt and Clark (2011) already pointed out the high variability in airborne magnetic signature.

    ~~**a** Subsurface interpretation based on magnetic, outcrops and drill hole data (Pawley and Wilson, 2019). Large mylonitic shear zones cross the area dominantly in a SW-NE direction. Strong influence on feature extraction is expected from plutonic bodies and mylonite zones. **b** Structural domains of the study area. The boundaries of the domains often coincide with~~
135  ~~crustal-scale shear zones. The location within the Gawler Craton of the area shown in this figure is indicated in Figure 1.~~
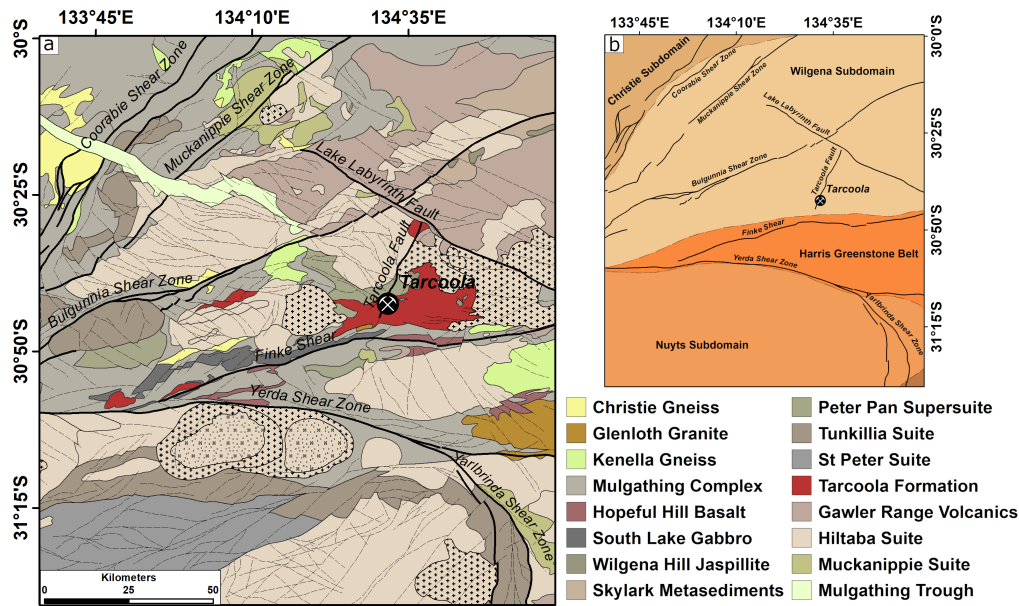
**Figure 2. a** Subsurface interpretation based on magnetic, outcrops, and drill hole data (Pawley and Wilson, 2019). Large mylonitic shear zones cross the area dominantly in a SW-NE direction. Strong influence on feature extraction is expected from plutonic bodies and mylonite zones. **b** Structural domains of the study area. The boundaries of the domains often coincide with crustal-scale shear zones. The location within the Gawler Craton of the area shown in this figure is indicated in Figure 1.

Overlying the crystalline basement of the Gawler Craton in the analysed area are Palaeozoic, Mesozoic and Cenozoic sedimentary sequences that combined form significant but variably thick cover ranging in thickness from 0 to ~~>600m~~more than 600 m. However, the spatial distribution of each sedimentary sequence is poorly understood (Hou, 2004).

The oldest preserved cover is ~~the~~ composed of Late Carboniferous to Early Permian post-glacial sediments within the Mulgathing Trough in the north-western corner of ~~Figure 2~~the study area (figure 2) (Nelson, 1976; Hibburt, 1995). Magnetic source depth analysis ~~reveals~~ suggests that the trough ~~could in places be~~ is more than 600~~metres~~ m deep, with the maximum depths ~~probably~~ likely not detected (Foss et al., 2019). The overall variability of the cover thickness in the study region is shown in Figure 4.

The terrain across most of the study area is relatively flat to moderately ~~undulating~~undulated. Prominent topographic highs are localised around dissected rocky outcrops. The surface is characterised either by aeolian sand covering variably weathered bedrock ~~, mostly~~ mainly in elevated parts of the landscape, or by saline playa lakes and drainage tracing topographic lows. One distinct feature is the longitudinal dunefield that occupies an extensive area in the south-western and southern part (Figure ~~??~~3) with individual ~~dunes over several kilometres in length and dune crest mainly trending~~ plurikilometric-long dunes with W-E trending crests.

## 2.2 Structural Framework
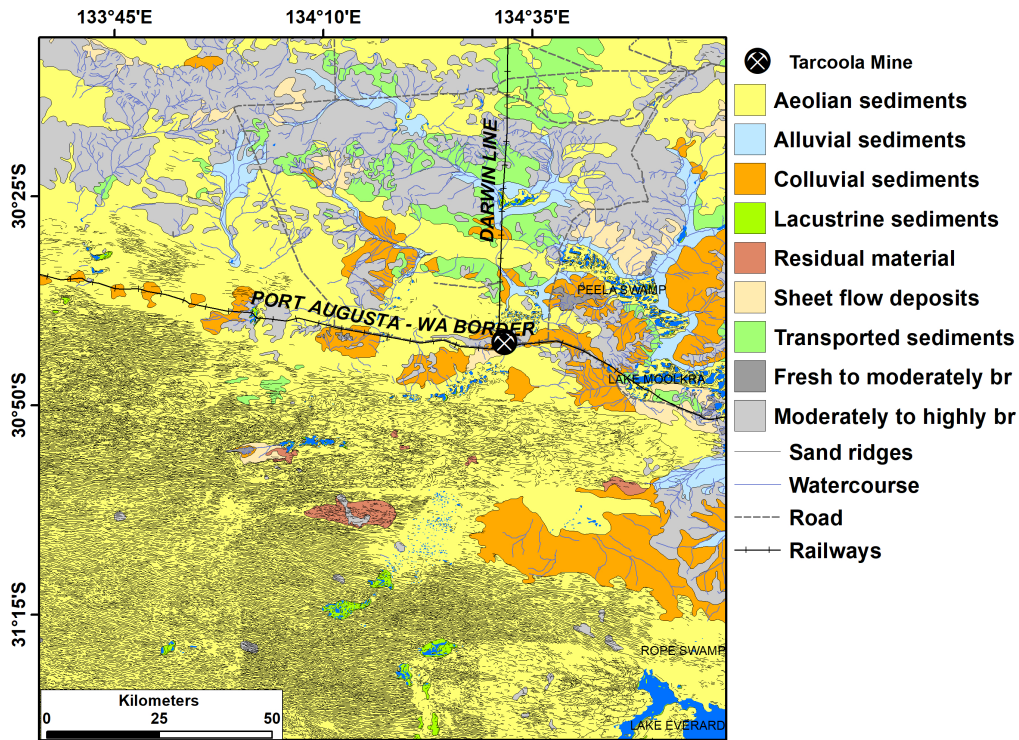
**Figure 3.** Surface feature map displaying regolith material (Krapf et al., 2012), roads, watercourses and sand ridges. Especially linear structures such as roads and sand ridges are expected to strongly influence the automated lineament extraction process.[br: bedrock]

~~A solid geology interpretation~~ An interpretation of the geological framework was undertaken around Tarcoola in the central Gawler Craton (Wilson et al., 2018; Pawley and Wilson, 2019) using the new GCAS aeromagnetic data (see figure 5c) that was collected between 2017 and 2018, at 60 m ground clearance with 200 m spacing on east-west flight lines (Foss et al., 2019). ~~It is possible to recognise two main types of linear geological structures~~ The dominant linear structures that can be identified in the aeromagnetic data ~~; namely~~ are shear zones and faults. ~~Shear zones are zones of relative displacement, where localised greater strain leads to ductile deformation. Shear zones can range from discrete planar structures to broader corridors of deformed and foliated rock. Faults are brittle fractures, or zones of fractures, which accommodate movement between two blocks of rock. Faults and shears can be recognised as~~ Identified faults and shears tend to be relatively discrete zones whose magnetic signature was altered by circulating fluids, or by the juxtapostion of two blocks of rock with different magnetic character. In general, the shear zones are prominent on aeromagnetic images as they form extensive structures that often separate lithological packages with contrasting magnetic character or are associated with changing trend of the magnetic grain (e.g. Figure 5c). Faults often form shorter, narrow features with changing magnetic expressions that can be difficult to recognise in rocks with low magnetic response. For details on the signature of fault in aeromagnetic data we refer to Grauch and Hudson (2007). The area in Figure 2 can be divided into a series of structural domains with distinct faults patterns~~.~~:
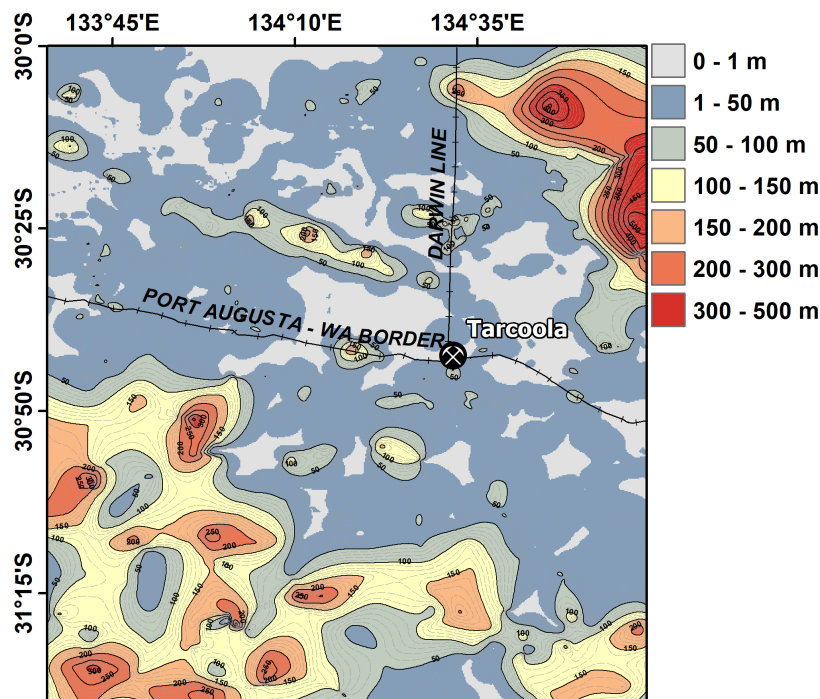
**Figure 4. a** ~~Surface feature map displaying regolith material (Krapf et al., 2012), roads, watercourses and sand ridges. Especially linear structures such as roads and sand ridges are expected to strongly influence the automated lineament extraction process.~~ **b** Depth to basement map (Cowley et al., 2018)~~.~~

165     Few faults are ~~recognised~~ identified in the Christie Domain, although this could be due to the bland magnetically low character of the region. One exception is the >80 km-long, northwest-trending Mulgathing Trough (Figure 2b), which can be recognised as it is filled with Permian glacial sediments that affect its magnetic response.

    The Wilgena Domain contains northwest-trending faults that are particularly prominent as narrow non-magnetic zones in the magnetic Hiltaba Granite plutons (Figure~~(~~ 2b). Some faults are relatively straight to curviplanar and can be traced for >80 km
170 (e.g. the Lake Labyrinth Fault), whereas others are shorter and form anastomosing and bifurcating structures. The northwest-trending faults typically show apparent dextral offset, and usually cut the major shear zones. An exception to this trend is the north-northeast-trending Tarcoola Fault that appears to propagate from the southern Finke Shear Zone.

    The faults form several patterns in the Nuyts Domain (Figure~~(~~ 2). To the northwest, the faults are northwest trending with dextral offset. The eastern Nuyts Domain is characterised by northeast-trending sinistral faults, aligned sub-parallel to the
175 Koonibba Shear Zone located to the southwest of Figure 2 (see detailed map in (González-Álvarez et al., 2020)). In the central Nuyts Domain, a ~~Hiltaba Suite pluton~~ pluton from the Hiltaba Suite has a long, straight northwest-trending margin that is bound by the Kooniba Shear Zone. The granite pluton adjacent to the shear is cut by abundant faults that ~~occur~~ are observed in several orientations and looks like a fracture zone. None of these faults extend across the Kooniba Shear Zone into the rocks of the St Peter Suite.

180 ~~In general, the shear zones are prominent on aeromagnetic images as they form extensive structures that often separate lithological packages with contrasting magnetic character or are associated with changing trend of the magnetic grain (~~The NW- and NE-trending faults across a large portion of the study area cut the $\approx$ 1585 Ma Hiltaba Suite plutons. Therefore, the faults formed at or after $\approx$ 1585 Ma, likely during Kararan Orogeny that occurred either at 1570 Ma (Hand et al., 2007) or 1600-1570 Ma (Reid et al., 2017, and references therein). There is evidence that pre-existing structures (i.e. ~~g. Figure 5c)~~

185 ~~. Faults often form shorter, narrow features with changing magnetic expressions that can be difficult to recognise in rocks with low magnetic response. For details on the signature of fault in aeromagnetic data we refer to Grauch and Hudson (2007)~~ Gulgunnia, Muckanippie, and Coorabie shear zones (see figure2) were reactivated during the Kararan Orogeny (Dir, 2005; Reid and Dutch, . In conclusion, most of the large-scale fault zones could have provided pathways for mineralizing fluids. Based on the observable offsets of pluton contacts a N-S directed shortening can be assumed during the formation of the Au-deposit

190 mentioned above.

## 3 Methodology

In the following section we introduce the datasets used for lineament extraction, then describe the lineament analysis we employ to compare lineaments extracted by different techniques, followed by a description of the three lineament extraction techniques used.

195 ### 3.1 Datasets

Lineaments extracted from a subset of the Gawler Craton Airborne Survey (GCAS), the world's largest high-resolution airborne geophysical and terrain imaging program at ~~200m~~ 200 m line spacing, were analysed by Foss et al. (2019). The data that is released under the Creative Commons Attribution 4.0 International Licence includes total magnetic intensity (TMI), radiometrics (RAD), and digital elevation model (DEM).

200 We utilized the ~~digital elevation model (DEM )~~ DEM derived from laser altimeter subtracted from differential GPS heights (Figure 5a), radiometric data (total dose) processed using the Noise Adjusted Singular Value Decomposition (NASVD)~~(Hovgaard and Grast~~ (Hovgaard and Grasty, 1997) (Figure 5b), total magnetic intensity reduced to pole (Figure 5c), and gravimetric data gridded to ~~100m~~ 100 m with a station spacing between ~~50m~~ 50 m and 50,~~000m~~ 000 m (Figure 5d).

The data presented is freely available through the South Australian Resources Information Geoserver SARIG (https://map.sarig.sa.gov.au

205 ### 3.2 Lineament analysis

Automated lineaments analysis allows for obtaining unbiased metrics for comparison of the data in terms of their dominant strike directions. For each dataset the principal orientations are automatically obtained. ~~For simplification we assume that the individual principal strike directions follow Gaussian distributions. We~~ Assuming that the strikes represents a multimodal distribution, we first calculate the kernel density estimation (kde) using normal distributed kernels. The kde is a non-parametric

210 estimator that basically smoothes each data point into a small density function based on the underlying kernel and bandwidth.
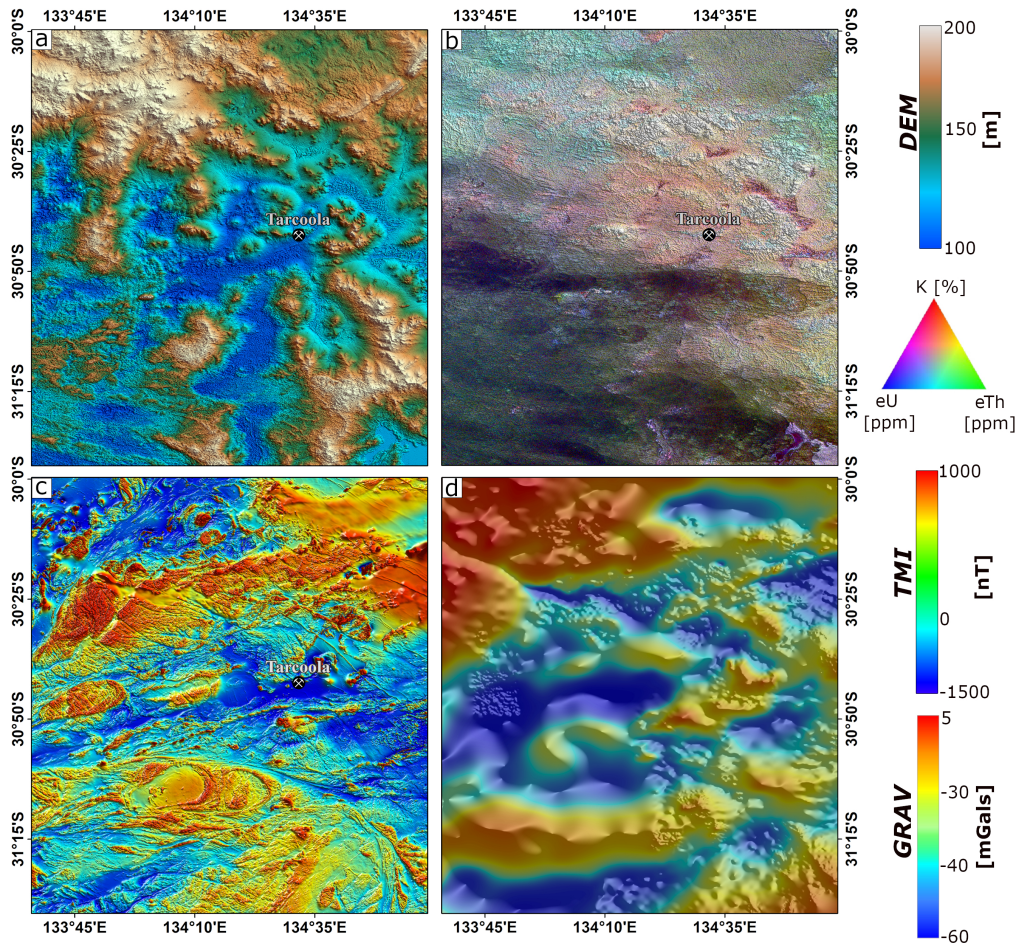
**Figure 5. a** Colour digital elevation model (laser altimeter) [min: 84.08 m; max: 365.33 m], **b** color radiometric dose rate (NASVD corrected) [min:0.074 nGy/hr; max: 239.30 nGy/hr], **c** color total magnetic intensity (reduced to pole) [min: -1978.16 nT; max: 21638.8 nT], and **d** color and hillshaded Bouguer Anomaly gravity image (Katona, 2017) [min: -158.15; max: 64.74]. Data source: GCAS Region 9A, SARIG 2020

The obtained kde function then represents the sum of all these subfunctions. By this we obtain an smoothed estimation of the distributions probability density function of the distribution. We then . This analysis was performed using the FracG software (Kelka and Westerlund, 2021). For a general overview on how kde works we refer to Chen (2017).

For simplification we assume that the individual principal strike directions follow Gaussian distributions. In this case, we obtain a best-fit model allowing for up to ten principal strike directions (Gaussinas) fitted to teh obtained kde. The parameters of the Gaussians are obtained via maximum likelihood fitting. Goodness-of-fit testing is performed iteratively based on a modified Akaike Information Criteria (Akaike, 1998). The amplitudes of the Gaussians are normalized and are proportional to the number of lineaments that belong to this distribution.

Figure 6 shows the principal orientations of the structural interpretation (Figure 2a). Raw kernel density estimates are plotted as a dotted line to which the Gaussian model is fit to. Clearly two perpendicular directions dominate the data with a subordinate set of roughly N-S striking lineaments.
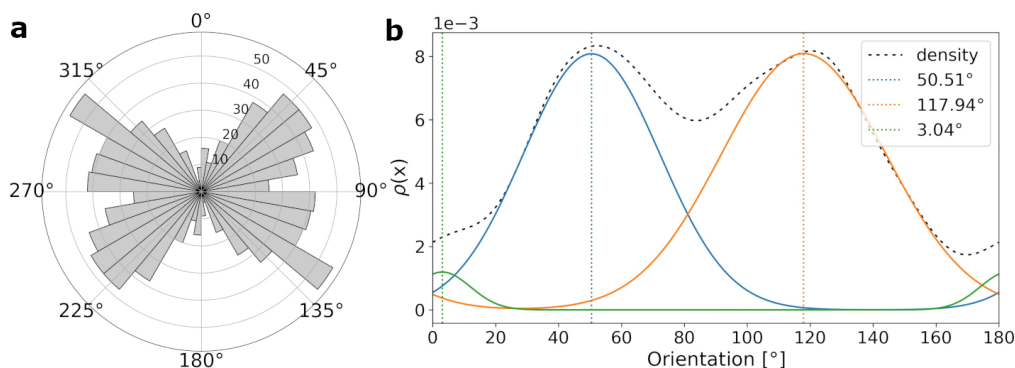
**Figure 6.** Directional analysis of structural interpretation (Figure 2a). **a** Rose diagram showing the distribution of strike directions of the ~~data~~ structural interpretation with a bin size of 10 degrees. **b** Gaussian distributions fitted to the probability density function of the strike directions obtained via kernel density estimation.

## 3.3 Manual lineament extraction

Lineaments are pattern breaks within data that the human eye can depict as a straight or somewhat-curved feature in an image (Boucher, 1997). This is dependent on the person's visual ability as well as technical experience and hence mapping the presence and location of surface lineaments can vary significantly between individuals. By applying different types of pre-processing (e.g. edge detection filtering, hill shading etc.) different features in the raster image can be enhanced thus leading to different lineament sets segmented from the same data set. Direct observation-based surface lineament mapping has been widely applied in geoscience and has been improved by the increasing availability of high-resolution satellite images as well as ~~digital elevation models (DEM )~~ DEM and Multi-resolution Valley Bottom Flatness (MrVBF) (Gallant and Dowling, 2003). Surface lineaments were manually mapped in the DEM (Figure 5a) by direct visual identification and digitisation in ArcGIS 10.6. Figure 7 shows the manually mapped lineaments in the DEM (a) and in the raster representing the mean gradient component (b). The mean gradient component was calculated as the arithmetic mean of the horizontal and vertical gradient components obtained though Sobel convolution filtering. ~~Based on the shape of the underlying kernel this~~ This edge detection filter ~~allows for obtaining~~ can utilize different kernels for enhancing edges of different orientation (e.g. horizontal or vertical) (Shrivakshan and Chandrasekar, 2012). The mean gradient component we calculated as a pre-processing step prior to the manual segmentation contains enhanced edges in horizontal and vertical orientation. The dominant orientation in both datasets is around 106 and 110 degrees, respectively. In both datasets three Gaussians provide the best fit, whereas the two subordinate directions of both data sets differ significantly.
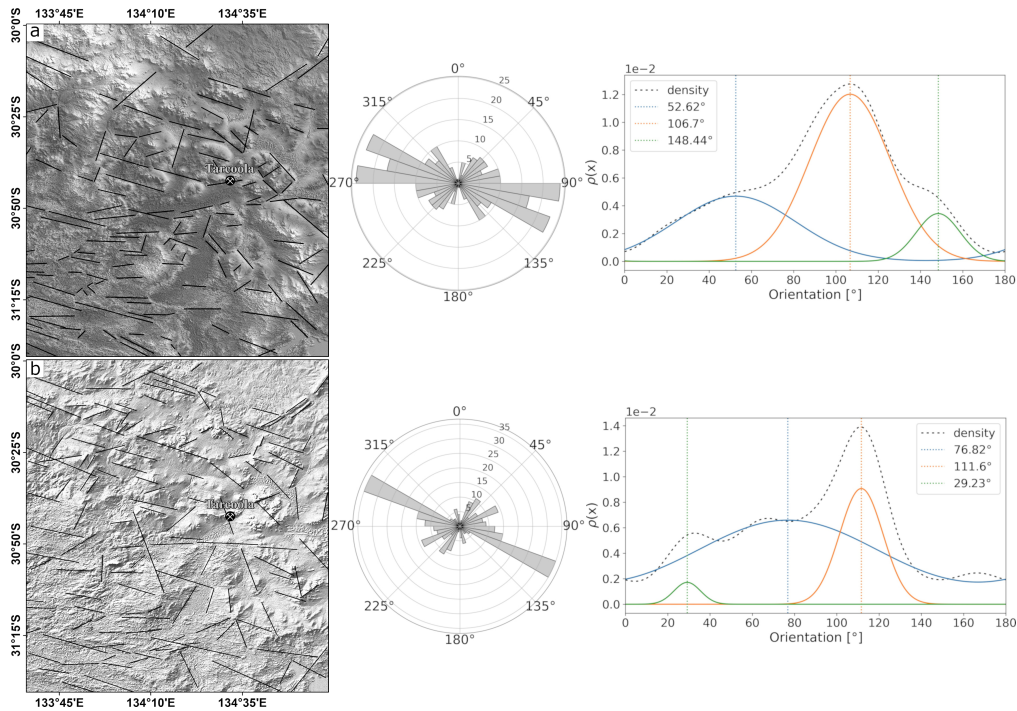
**Figure 7. a** Manually segmented lineaments observed in the unprocessed laser altimeter data. To the right of the map the rose diagram showing the distribution of strike directions (bin size of 10 degrees) and the Gaussian model fitted to probability density function is shown. **b** Manually segmented lineaments obtained from the laser altimeter data after edge detection filtering. We show the mean horizontal and vertical gradient components obtained via Sobel convolution filtering. To the right of the map the rose diagram shows the distribution of orientation with a bin size of 10 degrees and the lower plot represents the Gaussian models fitted to the probability density function.

## 3.4 Automatic Gradient Extraction (Worms)

240  A multi-scale edge detection technique has been applied to the potential field data which produces edge features called "multi-scale edges" (or colloquially "worms"). This technique (Holden et al., 2000; Hornby et al., 1999) relies on a wavelet transform based on the Green's function of vertical gravity or reduced-to-pole (RTP) total magnetic intensity. A low-resolution multi-scale edge mapping of the whole Gawler Craton was performed by Heath et al. (2009). Foss et al. (2019) applied a higher resolution mapping using the more recent GCAS Region 9A magnetic field data and updated gravity coverage.

245  The potential field data ~~is~~ was processed using upward continuation (UC) to generate edge features that can be considered representative of different depths. Upward continuation suppresses high frequencies in the data, and increases the weighting of signals from deeper physical property contrasts. Calculation of edge enhancement transforms at different upward continuation heights, producing a series of edge mappings ('multi-scale edges' or 'worms'). Edges derived from the gravity data map subsurface density contrasts, and those from the magnetic field data map subsurface magnetization contrasts. The edges (in particular the shallow edges) depend considerably on data distribution which is very regular for the magnetic field data, but

highly irregular for the gravity data. In areas of sparse gravity coverage, it is not possible to map detail in the shallow gravity multi-scale edges. In compensation, the gravity field better expresses contributions from deeper property contrasts than the magnetic field. However, the principle value of having multi-scale edges derived from both gravity and magnetic field data is that they map quite separate physical properties, even though both properties depend on lithology. In some cases the contact
255   between two lithologies is both a density and magnetization contrast, and the two multi-scale edge vectors are strongly corre-lated, but in other cases a lithology contact may cause only a significant density contrast or only a significant magnetization contrast, giving rise to edge vectors in only one of the fields. The combination of the two sets of edge vectors is therefore much more informative than either one alone. By their nature potential fields measured above a physical property interface are automatically smoother than the trace of that interface. They cannot include abrupt changes of trends and at higher upward
260   continuations the potential field and multi-scale edge expression of any straight-line property contrast becomes progressively more curved. There are therefore compromises in matching naturally curved multi-scale edges with corresponding straight lin-eaments extracted from the same dataset. The principal orientation of lineaments is roughly E-W for the gravity and magnetic data (Figure 8). The orientation exhibited by the gravity lineaments (Figure 8b) is uniform with one clear principal orientation. The lineaments derived from the magnetic data (Figure 8a) exhibit three main directions.

## 3.5   Automatic lineament extraction

Lineaments have also been extracted from the DEM, radiometrics, gravity, and magnetics using Geomatica's LINE func-tion (Geomatics, 2005). This technique relies on properties inherent to the image (e.g. pixel intensity) making use of Canny edge detection (Shrivakshan and Chandrasekar, 2012) as the basis.

The gradient of an image is computed and pixels that are not a local maximum are suppressed. Edge strength threshold of
270   pixels produces a binary image that, after applying a thinning algorithm, results in skeleton curves that represent edges. If a curve meets a minimum length criterion, the curve is approximated by line segments within an error threshold. Lineaments are the result of linking line segments if they have similar orientation.

PCI Geomatics defines a lineament as a "straight or somewhat-curved feature" (Geomatics, 2005) and the parameters control the extent to which edges detected in the image may result in a line feature. Originally intended to be used on
275   radar images, the technique has been widely used in various remote sensing applications (Pandey and Sharma, 2019, e.g.) (e.g., Pandey and Sharma, 2019)]. Edges identified relate to significant changes within a given image and the resulting linea-ments are highly dependent on user-specified parameters that control length and segment linkage. For detailed description of the parameters used in this study we refer to González-Álvarez et al. (2020) and Pawley et al. (2021).

The lineaments were automatically extracted for datasets representative of surface (Figure 9) and subsurface (Figure 10)
280   features. The surface data yields a single principal orientation of about 90 degrees in both lineament collections.

In contrast to the uniform distribution of lineament orientation obtained for the surface layers, the automatically detected subsurface lineaments exhibit two nearly equal principal directions for the total magnetic intensity (Figure 10a) and a more uniform distribution obtained for the gravity data (Figure 10b). The dominant direction in each subsurface dataset differs significantly and are oriented nearly perpendicular to each other.
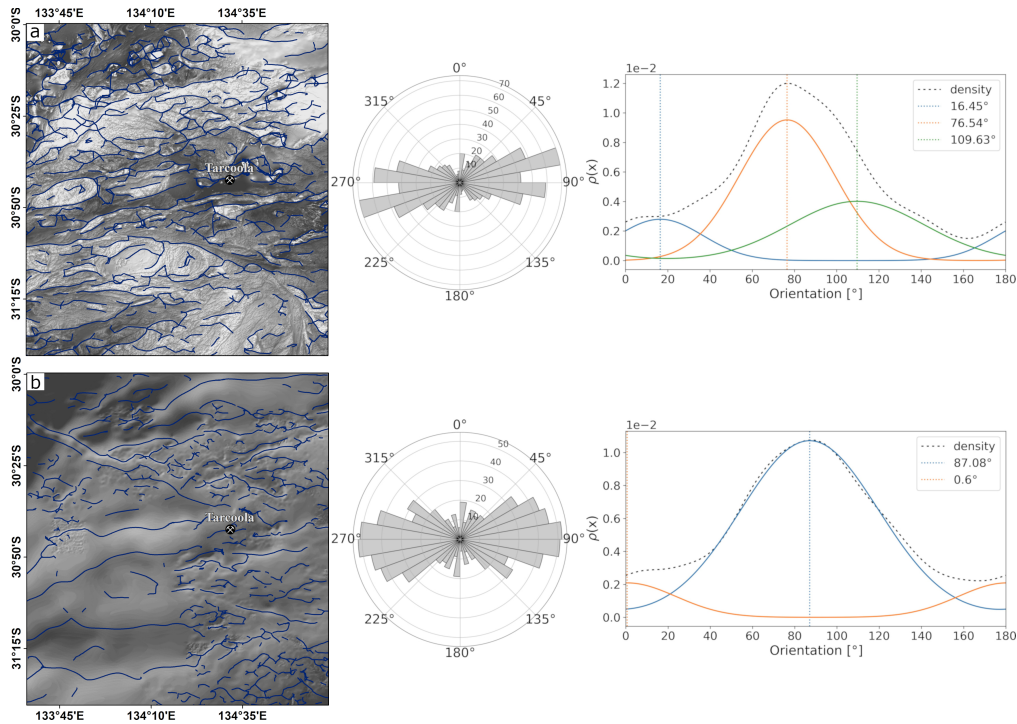
**Figure 8. a** Automatic gradient extraction with an upward continuation to ~~2070m~~ 2070 m performed on the total magnetic intensity after pole reduction. To the right of the map the rose diagram shows strike distribution with a bin size of 10 degrees and the Gaussian functions fitted to the probability density function are shown.

**b** Automatic gradient extraction with upward continuation to ~~930m~~ 930 m for gravity data. To the right the rose diagram visualizing the orientation distribution and the model fitted to the probability density function are shown. Upward continuation heights of the gravity and magnetic data were selected such that the lineaments represent similar detail.

## 4    Comparison of lineament datasets

The lineament datasets from the three techniques applied differ the most in terms of their length distribution (Figure 11a). In particular, the automatically ~~segmented~~ generated surface lineaments exhibit a narrow distribution with the highest density limited to regions around the mean and median. The length distributions of the lineaments automatically extracted from the subsurface data show a wider range slightly skewed towards smaller values. It is worth noting that the length tolerance of lineaments is an input parameter and the bias is well represented in the resulting lineament datasets. The automatic gradient extraction ('worms') ~~yield~~ yields more distributed length of lineaments where smaller lineaments dominate the data. Manually extracted lineaments show a similar length distribution independent of whether the interpretation was performed on the processed or unprocessed elevation data. The structural interpretation that was performed mainly on the total magnetic intensity data exhibits the widest distribution. We note that the different techniques will yield variable results and different information can therefore be obtained from the same dataset by applying for instance the worming (figure 8) or automatic segmentation
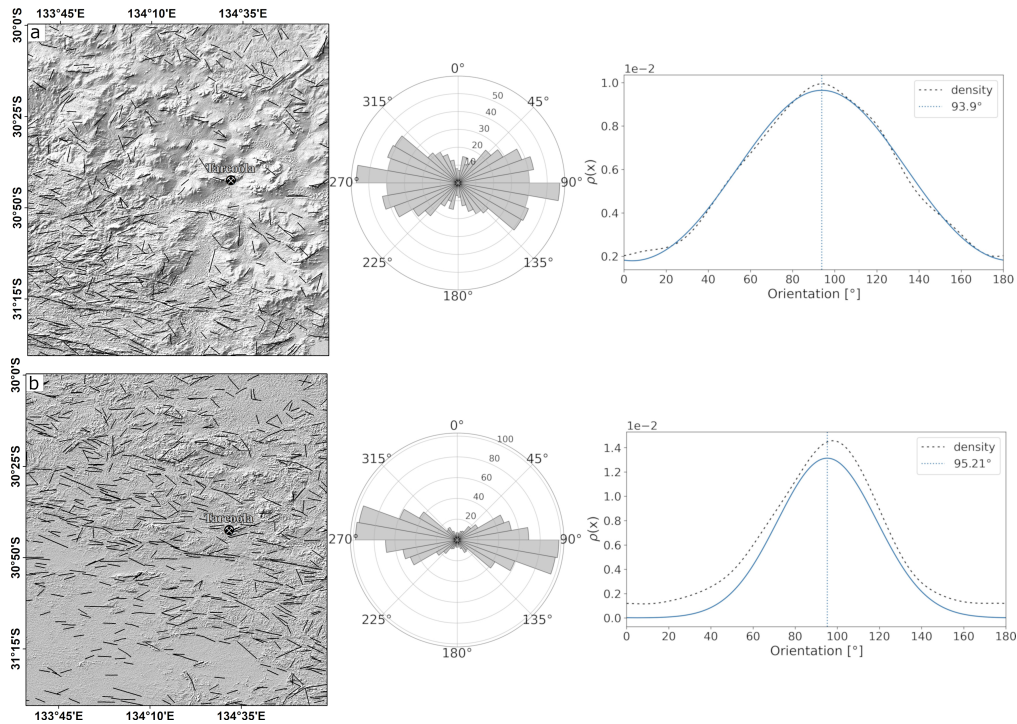
**Figure 9.** Lineaments detected by PCI Geomatica's LINE module in (**a**) the laser altimeter data and in (**b**) the radiometric data (total dose rate). The base map is the mean gradient component of the respective data set used for visualization purposes only. To the right the rose diagram and the models fitted to the probability density function are shown for each data set (bin size of 10 degrees).

(figure 10). We do not seek to compare the geological or physical information inherent to each dataset but rather perform a statistical analysis to point out the most striking geometrical differences (e.g., length and orientation). An in-depth evaluation of which extraction methods yields more reliable or realistic geological information is beyond the scope of this study.

The principal strikes exhibit a common E-W trends in the surface and subsurface datasets (Figure 11a&b). The dominant orientations of the surface lineaments (Figure 11b) scatter around the E-W plane with only one subordinate orientation that is somewhat oriented perpendicular (line labelled 4: automatically extracted from radiometric data). The orientations of the subsurface lineaments are more diverse but also scatter mainly around the E-W plane. Subordinate orientations are more common in the subsurface lineament datasets and most pronounced in the worms (Figure 8a&b) and in the lineaments automatically extracted from the total magnetic intensity (Figure 10a). The latter exhibits a bimodal distribution that is comparable to the manual structural interpretation (Figure 6). Overall, the automatically extracted surface lineaments tend to yield uniform distributions for length and orientation whereas the automatically extracted subsurface lineaments exhibit wider length distributions and non-uniform strike directions. The automatic gradient extraction produces lineament sets with wider length distributions and orientations dominated by an E-W trend with subordinate orientations that are nearly perpendicular to the principal strike. Apart from the manual structural interpretation, this method is the only one presented in this study that produces strongly
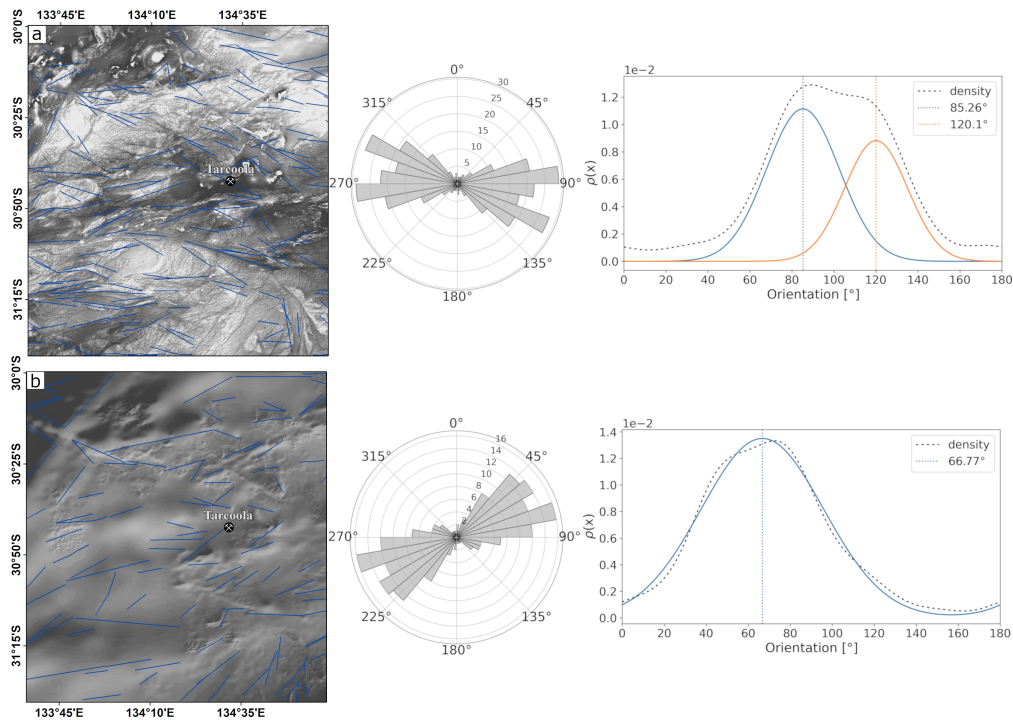
**Figure 10.** Lineaments automatically extracted with PCI Geomatica LINE module from the total magnetic intensity (reduced to pole) (**a**) and the gridded gravity data (**b**). To the right of the maps the rose diagrams show the orientation distribution (bin size of 10 degrees) and the models fitted to the probability density of the empirical data.

curved lineaments. Lineaments that are manually extracted show a comparable length distribution independent of whether the data was processed by edge detection filtering. The locations and orientations are influenced by the processing and so is the number of features (Figure 7a&b). In summary, a dominant orientation trend is observable in the automatically generated surface and subsurface lineaments that is roughly east-west. Only the manually extracted surface lineament set shown in Figure 7b and the structural interpretation (Figure 6) exhibit considerable divergence from this orientation. The main difference between the different lineament sets is demonstrated by their length distributions (Figure 10 ).

## 5  Lineament density maps as an ~~Exploration Tool~~exploration tool

Here we present a workflow for exploration targeting based on lineament density and intersection density per unit area that utilizes remotely sensed surface and subsurface data. Density maps are calculated for several combinations of surface and subsurface layers. Two types of density maps deriving potential exploration targeting areas are:

- Density maps of lineaments per area (P20)
- Density maps of ~~lineaments~~ lineament intersections per area (I20)
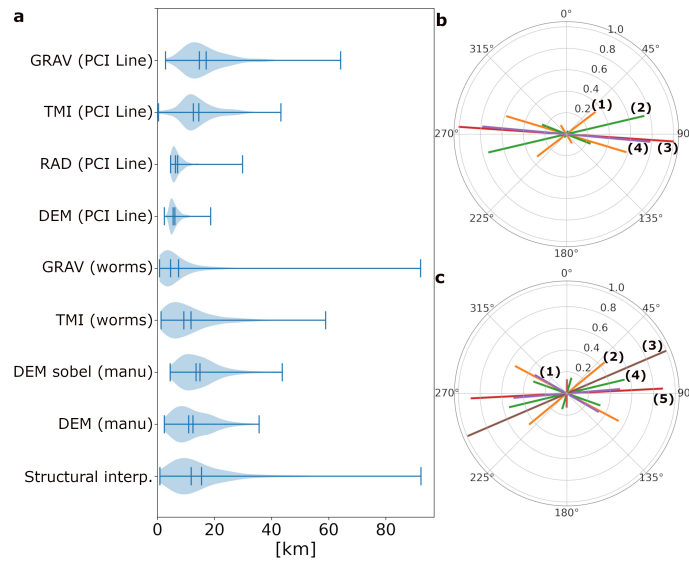
**Figure 11. a** Violin plots showing kernel density estimates of the lineament length distributions. Minimum and maximum values, mean and median are shown as vertical lines for each distribution. Plots were generated using the python library Matplotlib **b** Principal orientations of surface data sets derived by fitting Gaussian distributions to the data [*1*: manual interpretation of laser altimeter; *2*: manual interpretation of Sobel filtered laser altimeter; *3*: automatic detection in laser altimeter data; *4*: automatic detection in radiometric data (total dose count)]. **c** Principal orientation of subsurface data sets obtained via fitting Gaussian distributions to the data [*1*: Automatic detection in TMI; *2*: Structural Interpretation; *3*: Automatic detection in gravity data; *4*: TMI worms (UC 2070); *5*: Gravity worms (UC 930)]. In both rose diagrams the length of the lines corresponds to the amplitude of the Gaussians respectively.

~~Datasets~~ Lineament datasets that are obtained with the same method and correspond to signals either both from the surface or both from the subsurface are merged (see tables reftab01 and 2). The aim of this analysis is to identify areas of maximum line density and intersections in surface and subsurface signals in one dataset. The merged datasets with their name used in this section are shown in table 1.

P20 maps represent the number of lineaments per unit area derived for rectangular sampling windows of size ~~2kmx2km~~ 2 km by 2 km. The pixel resolution of the derived raster file is set to the search window size. I20 maps are derived by converting the lineament data into a graph representation where intersections between lineaments are vertices (Sanderson et al., 2019). The number of intersections is derived using a pixel size of ~~2km by 2km~~ 2 km by 2 km and circular sampling windows with a radius of 2.5 km. The maps are then up-sampled via bilinear interpolation to a cell size of 500~~by 500m. For further details on the lineament analysis the reader is referred to Kelka et al. (2021)~~ m by 500 m. The software is open-source Kelka and Westerlund (2021).

The targeting maps are derived by overlaying the P20 maps with contours of the I20 maps (Figures 12, 13,and 14). ~~As athreshold for identifying~~ We used combined lineament dataset that represent either surface or subsurface signals (see table 1). In cases where we utilized the structural interpretation (figure 2) as the subsurface datasets the density maps comprise three individual lineament datasets (figures 12 and 13 a) whereas the other targeting maps comprise of four lineaments sets

**Merged datasets**

| Name | Segmentation method | Dataset 1 | Dataset 2 |
|---|---|---|---|
| Surface manual | Manual segmentation | DEM (Figure 7a) | DEM mean gradient (Figure 7b) |
| Surface auto | ~~Laser altimeter~~ PCI Line module | DEM(Figure ~~13~~9a) | Radiometrics DR (Figure ~~13~~9b) |
| Subsurface worms | ~~TMI UC 2070m~~ Ridge detection (worming) | TMI UC 207 0m (Figure ~~10~~8a) | Gravity UC ~~930m~~ 930 m (Figure ~~10~~8b) |
| Subsurface auto | PCI Line module | TMI RTP (Figure ~~13~~10c) | Gravity (Figure ~~13~~10d) |

**Table 1.** Merged datasets corresponding to surface and subsurface signals obtained with the same method.

(figures 13 d, 14). The reason behind this is that the remotely sensed data sets comprise two datasets for the surface (DEM and radiometrics) and two datasets representing subsurface (TMI and gravity) respectively that might detect features at different scales or are based on data of different resolutions. We merged the lineament sets to obtain comprehensive datasets comprising surface and subsurface features. Which datasets are used for obtaining the respective targeting map and which extraction

340 methods were used for obtaining the utilized lineaments is summarized in table 2. We further classified the targeting maps into "manual", "automatic", or "semiautomatic" indicating whether the underlying lineament sets were derived with purely manual segmentation, represent a combination of manually and automatically extraction or are obtained solely by automatic segmentation (see table 2).

Considering not only the overall lineament density but also the intersection density allows us to further constrain potential

345 targeting areas. By obtaining intersection densities, cross-strike features can be identified that are thought to represent zones of enhanced permeability (Wheeler, 1980; Southworth, 1985). Areas of enhanced structural complexity or numbers of cross-strike discontinuities could therefore represent zones for preferential up-welling of mineralizing fluids, and we suggest that the adjacent areas that comprise an overall high density of lineaments represent preferential exploration targets. For identifying these mineral potential zones, we set a threshold of 9 intersections per ~~500m by 500m~~ 500 m by 500 m pixel size and then

350 visually identified the areas of overall high densities in the vicinity of these specific points as favourable targeting areas. The threshold is kept constant across datasets in this study to ensure a better comparability but would need to be adjusted depending on the underlying data for more reliable targeting. We collate the different lineament sets that are derived automatically or manually into automatic, manual or semi-automatic datasets (see table 1).
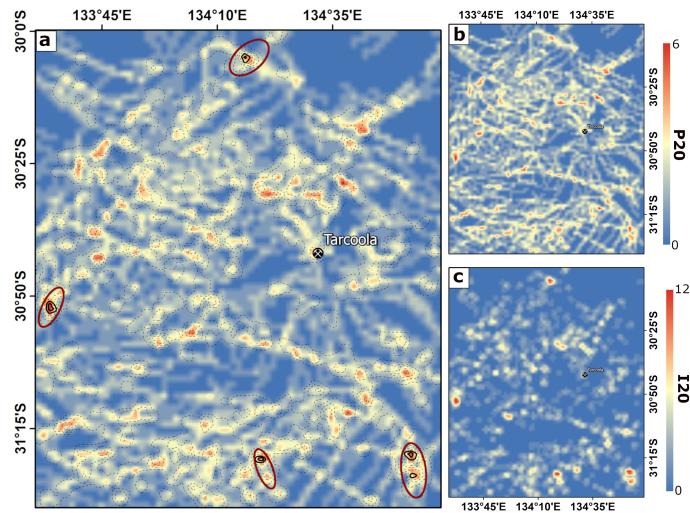
**Figure 12. a** Targeting map derived from "Surface manual" combined with the structural interpretation (Figure 2a). **b** Lineament density map (P20). **c** Intersection density map (I20). Potential targeting areas that are indicated by red ellipses.

**Targeting datasets**

| Name (figure 15) | Segmentation methods | Merged Dataset 1 | Merged Dataset 2 |
|---|---|---|---|
| Manual | Manual segmentation | Surface manual (figure 7) | Structural interpretation (figure 2) |
| Semiautomatic (1) | PCI Line & Manual segmentation | Surface auto (figure 9) | Structural interpretation (figure 2) |
| Semiautomatic (2) | Manual segmentation & worming | Surface manual (figure 7) | Subsurface worms (figure 8) |
| Automatic (1) | PCI Line & worming | Surface auto (figure 9) | Subsurface worms (figure 8) |
| Automatic (2) | PCI Line | Surface auto (figure 9) | Subsurface auto (figure 10) |

**Table 2.** Summary of the targeting dataset (figures 12, 13, and 14) and name convention used in the combined targeting map (figure 15).

## 6 Discussion

355 This is the first study to utilize the newly acquired high-resolution dataset of South Australia (GCAS Region 9A (Childara)) to investigate the applicability of lineament mapping/extraction from a variety of data sets as a potential exploration tool. As both manual and automatic lineament extraction methods are subject to bias, we first compared the results obtained from both approaches.
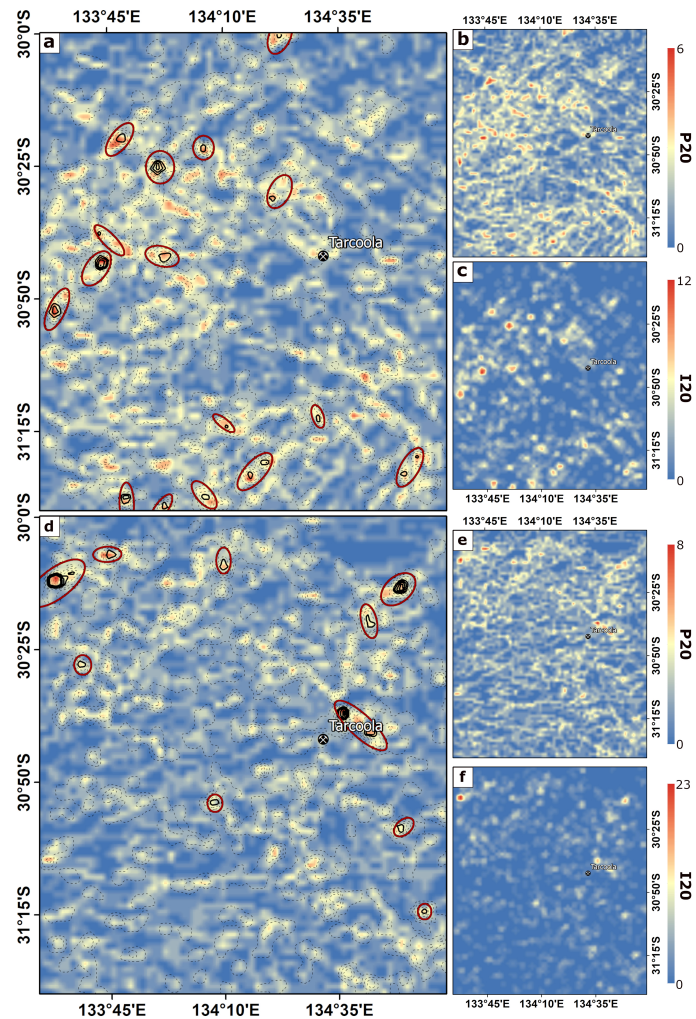
**Figure 13. a** Targeting map derived from "Surface auto" and the structural interpretation. **b** Lineament density map (P20). **c** Intersection density map (I20).

**d** Targeting map derived from "surface manual" and the "subsurface worm"). **e** Lineament density map (P20). **f** Intersection density map (I20). Potential targeting areas that are indicated by red ellipses.

During manual interpretation bias arises from subjectivity that is introduced by different interpreters (Raghavan et al., 1993)

360 and can also be caused by scale or variable processing techniques for edge enhancement such as illumination azimuth (Scheiber et al., 2015; Masoud and Koike, 2017). We do not seek to explore these aspects, but do note that interpretation bias may be playing a role in creation of the manual lineament dataset used. Automatic mapping methods can also be subjected to bias related to the type of applied edge detection filter and underlying segmentation algorithm. We applied the lineament extraction algorithm from the commercial software PCI Geomatica, as one of the main topics of this study is comparing
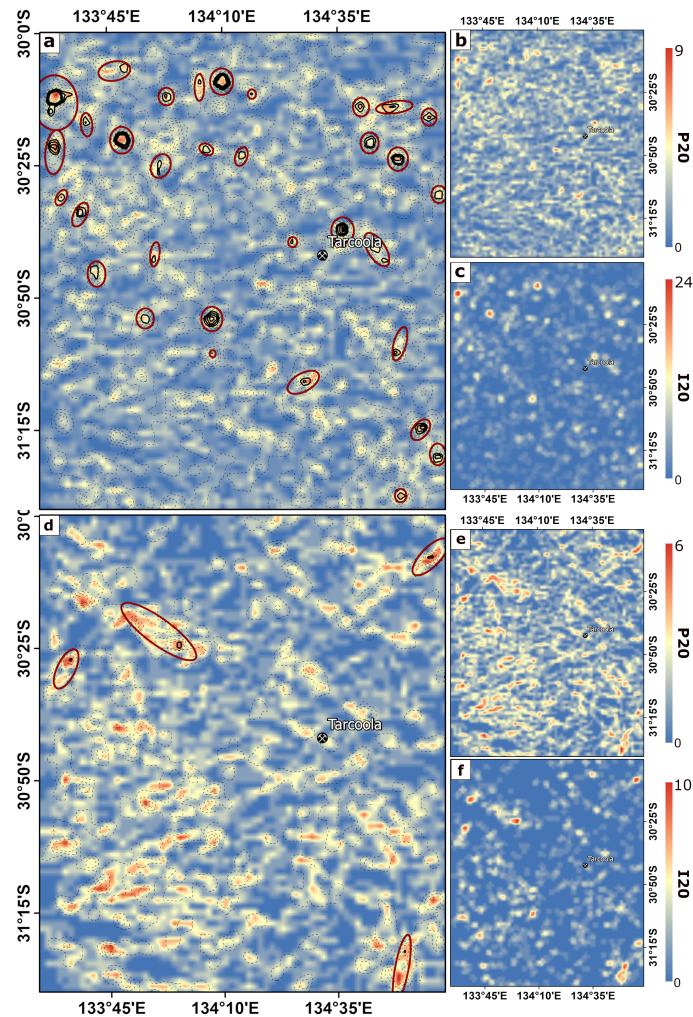
**Figure 14. a** Targeting map derived from "surface auto" and the "subsurface worms". **b** Lineament density map (P20). **c** Intersection density map (I20).

**d** Targeting map derived from "surface auto" and the "subsurface auto"). **e** Lineament density map (P20). **f** Intersection density map (I20).

Potential targeting areas that are located at the margins of the domain indicated by red ellipses.

365    different conventional methods with automatic detection methods. Some input parameters of PCI Geomaticas LINE module will certainly introduce a bias towards certain length distribution of the extracted lineaments. The two most important parameter are the threshold to length and the threshold to angular difference that defines the maximum difference in orientations for uniting two segments (see table 7 in Kelka and Martinez (2019) for details on the parameters). We note that recently several new approaches were suggested for automatic lineament mapping (Zhang et al., 2006; Hashim et al., 2013; Xu et al., 2020;

370    Mohammadpour et al., 2020, e.g.) and utilizing one of these might yield results different to the ones presented here.
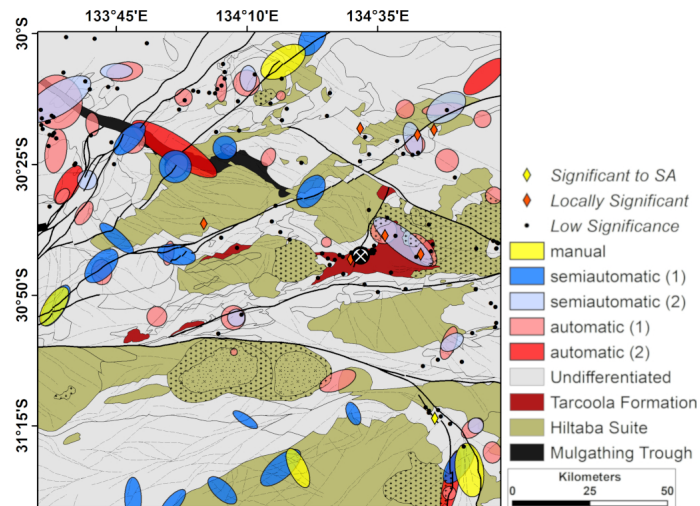
**Figure 15.** Geological and structural map showing the target areas identified by different combinations of lineament sets. In the legend manual refers to datasets that are ~~divide~~ divided solely through expert interpretation (Figure 12), semiautomatic represents datasets that are a combination of manually interpreted data (Figure 13) and automatic refers fully automatically extracted lineament data (Figure 14). Yellow and red diamonds indicate state-wide (SA: South Australia) and locally significant mineral occurrences that were detected in drill cores. The black dots are mineralizations that are below economic significance. The legend for the geological and structural units is shown in Figure 2a.

We will first discuss the similarities and differences of the surface and subsurface lineaments sets obtained with the different methods pointing out the individual strength or weaknesses. Lineaments obtained by manual mapping in this study scatter around a particular length (Figure 11)~~which is likely to be a result of human bias~~. The length distribution of automatically extracted surface lineaments is even narrower pointing towards a bias in lineament detection potentially related to the parameter
375  combination applied for automatic mapping (see section 3.5). One other major difference is that the manual mappings yield three main directions for each data set whereas the automatic detection exhibits uniform distributions. The principal orientation of automatically and manually extracted lineaments are similar for the radiometrics and laser DEM, respectively, but differ by a maximum of 18°between the methods when compared to the dominant directions obtained from the manually derived lineaments.
380  The automatic detection method yields data that is more representative for local scale geomorphological features visible by the strong influence of the sand ridges in the southwestern part. In contrast, a human interpreter tends to identify the general trends in the data ~~and~~ where results can be biased by the preprocessing of the data such as edge enhancement filtering. In summary, a general trend of superficial features extracted automatically and manually scatter around a E-W to NNW-ESE direction and therefore this orientation is likely a characteristic regional feature of the cover across the investigated area.
385  Whether automatic lineament extraction is superior to manual mapping cannot be stated with certainty based on the data presented in this study. Choosing one method over the other might depend on the type and the thickness of cover. Generally human investigators identify more regional trends, which are probably hard to detect automatically. The reason behind this is

that a human interpreter will ~~detect the conscious~~ consciously detect the trends of lineaments and will merge them even if there are large gaps between the identified edges.

Geophysical lineaments are obtained from the gravity and magnetic data via automatic gradient extraction. The lineaments obtained from each geophysical dataset differ significantly in terms of length distribution and principal orientation (Figure 8). This could be attributed to different depths the upward continuation represent but is more likely to reflect the difference in resolution of the data and the physical properties each dataset is sensitive to. The gravity data yields lineaments that are attributed to major lithological boundaries pronounced by density contrasts. In the study region the prominent boundaries are the margins of the domains that often coincide with large crustal-scale shears and the Mulgathing Trough in the northwest (see Figures 2a& b). While the major crustal scale elements are traced by the lineaments extracted from the gravity data, the lineaments obtained from the magnetic data seem to reveal a more detailed picture of the subsurface structural framework. In addition to domain boundaries the magnetic lineaments also outline large intrusive bodies. In line with the the structural interpretation, three main directions are detectable for the magnetic "worms" (Figures 2&6) but only two for the gravity "worms" (Figure 8). While the edge vector's orientation and length distributions ~~differer~~ differ significantly, a reasonable correlation considering their locations is observable (Figure 8). In line with Foss et al. (2019), this suggests that the mapping of gravity and magnetic contrasts with worms allows for correlating the magnetic and gravity field anomalies. It must be pointed out that the mapped edges only act as approximate markers of the horizontal contrasts in density or magnetisation (Foss et al., 2019).

~~We note that, the~~ The presence of magnetic remanence may alter the field anomaly, rendering the reduction-to-pole data we used less useful~~, however~~. However, for our purposes of extracting lineaments from multiple datasets, the uncertainty in the degree of magnetic remanence is of less concern ~~than~~ compared to the uncertainty associated with the different automated and manual techniques in extracting lineaments. We note that the magnetic and gravity datasets are of different resolution and in particular the resolution of the gravity dataset is non-uniform. As the upward continuation acts similar to a low-pass filter the difference in resolution becomes negligible.

Automatic lineament mapping performed with PCI Geomatica (Geomatics, 2005) yields a picture less consistent with the structural interpretation of the subsurface framework. While the automatically extracted gravity lineaments still outline some crustal-scale boundaries (especially evident for the graben structure in the northwest) the information associated with the automatically extracted geophysical lineaments is inferior compared to the information that can be obtained by automatic gradient extraction and the latter method should be favoured for the mapping of geophysical lineaments. The "worms" trace the subsurface in greater detail and profound physical meaning can easily be attributed to the location of the lineaments as they are associated with strong lithology contrasts within the basement units. In contrast, the automatically extracted lineaments pick up a rough impression of the structural framework of the subsurface with only major elements detectable in the data, such as major shear zones and the Permian graben. We conclude that automatic gradient extraction is the superior technique for extracting geophysical lineaments from high resolution magnetic data and from gravity data with variable resolution.

In section 5 we tested an approach that integrates surface and subsurface lineaments in a simple framework for exploration targeting that is based on identifying areas of high lineament density and high intersection density. The justification for this

approach is that welling of hydrothermal fluids is often associated with structurally complex zones that comprise a high intersection density (e.g. Dimmen et al., 2017). Areas comprising an overall high density of discontinuities that are adjacent to

425 such zones of high structural complexity represent preferential exploration targets for hydrothermal mineralization. By combining surface and subsurface datasets we not only account for intersections in subsurface datasets but also for intersection of subsurface and surface lineaments. Such cross-strike discontinuities are an additional indicator for structurally complex zones and are taken into account in our workflow.

Especially in areas that comprise thick cover narrowing down potential exploration areas with an automatic or semi-automatic

430 method can significantly reduce cost for exploration. However, a great challenge is that surface impressions of basement hosted displacement structures can be offset compared to the location of the large-scale discontinuity in the basement. Furthermore, cross-strike features are likely associated with small scale shears that will not be traceable in potential field data that images basement structures. A reliable interpretation of surface and subsurface lineament sets is particularity challenging in an old crustal block such as the Gawler Craton and we consider the work presented here as an first attempt to unify a lineament-based

435 workflow for exploration targeting in such an environment.

Figure 15 shows the target areas identified by the different methods. At the current stage the areas identified as potential targets by different methods represent the most promising regions for follow up hydrogeochemical sampling for identifying mineral footprints in the cover. These are probably northeast of the Tarcoola mining site at the margins of a large intrusive body, in the northwestern part where the edge of Permian graben is cross-cutting the Muckamippie Shear Zone, the region in

440 the southeast close to the Yarlbrinda Shear zone, and the area in the northeast where mineral occurrences are reported along the Bulgunnia Shear Zone. Most of the targeting areas are located along the shear zones that form the borders of the geotectonic provinces. Giving that the area is part of the central Gawler gold province where mineralization are is mainly shear-hosted Au (Hand et al., 2007, and references therein) this seems to be in-line with the existing knowledge of the region. In addition, the targeting areas are often associated with the margins of the Hiltaba Suite (in particular in the southern part of Figure 15).

445 Here it is important to note that the gold deposits in the central Gawler Craton exhibit some similar characteristics considering the mineralization style, as the gold is dominantly hosted in sulphide-poor structurally controlled quartz veins that seem to be spatially related to the Hiltabas Suite (Daly, 1993). We do not directly identify the deposit exploited at the Tarcoola mine but an area to the northeast that is situated along the margin of the Tarcoola formation (know known host-rock (Pawley and Wilson, 2019)) that includes two known mineral occurrences of local significance.

450 Uncertainty in manual lineament mapping is directly related to the person's experience and the scale they are intending on mapping. The manual extraction of lineaments in this study focused on the regional linear trends (lineament greater than 1km 1 km). Addressing uncertainty for the automatic lineament mapping is hard difficult and directly related to the resolution of the underlying datasets. In case of the automatic gradient extraction, the upward continuation can pose another source of uncertainty related to the loss of detail that increases with higher upward continuations. For an example of how uncertainly

455 uncertainty in lineament mapping can be assesses statistically, we refer to Pawley et al. (2021). For a reliable interpretation of the obtained lineament maps the geological history of the respective area must be considered. This means that differently oriented lineament sets could correspond to different tectonic and fluid flow events. In areas comprising multiphase deformation

some extracted lineaments might therefore not be of relevance for the targeted mineral system and, for instance, directional constraints on the utilized lineaments would need to be applied. In the case study presented here, the youngest orogenic event (Kararan Orogeny) is thought to be linked to the mineralization (Bockmann et al., 2019; Fraser et al., 2007) and to the reactivation of pre-existing structures (Dir, 2005; Reid and Dutch, 2015). In this special case there is no need for applying strict constrains on the extracted lineament sets but this might be necessary for other regions.

We note that relatively few ~~know~~ known mineralization coincides with the targets identified by the lineament analysis (Figure 15) and further research is needed to validate the reliability of the presented workflow. Geological knowledge of the area might help to reduce the number of false positives obtained by lineament-based exploration targeting.

## 7 Conclusion

In this study we pointed out the differences between subsurface and surface lineaments in the Gawler Craton in South Australia mapped/extracted with different methods and from a variety of remotely sensed and geophysical data. We determined the principal orientations of each dataset by automatically deriving a best-fit Gaussian model of the data. Overall an E-W direction dominates in surface and subsurface datasets that likely represent the structural grain of the area. Surface lineaments manually mapped are clearly subjective and can be biased due to preprocessing of the data. Compared to automatic extraction the main difference seems to be the scale on which the extracted lineaments play a role; the manual interpretation picks up regional scale trends whereas automatically extracted features represent smaller scale, locally relevant structures. We found that the automatic gradient extraction ("worming") is superior to automatic lineament extraction performed with PCI Geomatica as the worms detect more details that are related to lithological and structural contrast. In this study we showed that automatic gradient extraction yields geophysical lineaments associated with a profound geological meaning compared to automatically detected edges. In terms of the surface lineaments we conclude that the automatic extraction represents a method that picks up more local scale features and is likely well suited for well exposed areas. However, in areas that comprise a thick, reworked cover manual mapping of lineaments yield a more regional scale picture and seems to represent a reliable method.

An integrated workflow that utilizes surface and subsurface lineaments should include density per unit area and intersection density per unit area. We found that a combination of geophysical lineaments derived by automatic gradient extraction combined with either manually or automatically mapped surface lineaments represents the most promising combination of data for exploration targeting. On one hand, the gravity and magnetic worms will coincide with present lithological boundaries or major structural features. To clearly state whether edges or lineaments observable in the surface data are correlated with crustal scale features such as shear zones requires further research. For efficiently combining intersection density and line density for targeting, spatial clustering algorithms might yield more reliable results compared to the simple approach presented in this study. The crucial parameters will be setting an appropriate threshold for intersection and line density for determining target areas.

*Code and data availability.* Datasets and the code for automatic lineament analysis are freely available:

490     South Australian Resources Information Gateway - https://map.sarig.sa.gov.au/ (Data).

    FracG - https://bitbucket.csiro.au/scm/fracg/fracg.git (Code).

*Author contributions.* Ulrich Kelka wrote the manuscript with input from all authors, analysed the data, and developed the computational framework. Cercia Martinez wrote parts of the manuscript, analysed data, performed the automatic extraction of lineaments, and revised the manuscript. Carmen Krapf devised the project, wrote parts of the manuscript, performed the manual lineaments extraction, and revised

495     the manuscript. Stefan Westerlund developed the computational framework, helped with data visualization, and revised the manuscript. Ignacio Gonzalez-Alvarez devised the project, helped with data interpretation, and revised the manuscript. Mark Pawley wrote parts of the manuscript, performed the structural interpretation, helped with data interpretation, and revised the manuscript. Clive Foss performed the automatic gradient extraction for the geophysical datasets, helped with interpretation, and revised the manuscript

*Competing interests.* The authors declare no competing interests and to have obtained permission to publish from CSIRO and the Geological

500     Survey of South Australia.

*Acknowledgements.* The work performed is with support from the Geological Survey of South Australia, and the provision of high-resolution airborne geophysical and terrain data for Region 9A from the Gawler Craton Airborne Survey (GCAS) by Laz Katona and Jonathan Irvine. Carmen Krapf and Mark Pawley publish with the permission of the Director of the Geological Survey of South Australia.

    Thanks to the Leadership team of the CSIRO Deep Earth Imaging Future Science Platform for supporting this collaboration with CSIRO's

505     Mineral Resources Business Unit.

    We thank the ~~two anonymous reviewers fro~~ four anonymous reviewers for their thorough revision which helped to improve this manuscript.

# References

Architecture of Proterozoic shear zones in the Christie Domain, western Gawler Craton, Australia: Geophysical appraisal of a poorly exposed orogenic terrane, Precambrian Research, 142, 28–44, https://doi.org/https://doi.org/10.1016/j.precamres.2005.09.007, 2005.

Akaike, H.: Information theory and an extension of the maximum likelihood principle, in: Selected papers of Hirotugu Akaike, pp. 199–213, Springer, 1998.

Bockmann, M., Wilson, T., Pawlery, M., Payne, J., and Dutch, R.: LA–ICP–MS geochronology from the Tarcoola Goldfield region, 2018–2019, Report Book 2019/00015, 2019.

Boucher, R.: Lineament Tectonic Data, South Australia, with a Focus on the Cooper Basin, Report Book 9739, 1997.

Budd, A. and Fraser, G.: Geological relationships and 40Ar/39Ar age constraints on gold mineralisation at Tarcoola, central Gawler gold province, South Australia, Australian Journal of Earth Sciences, 51, 685–699, 2004.

Chen, Y.-C.: A tutorial on kernel density estimation and recent advances, Biostatistics & Epidemiology, 1, 161–187, 2017.

Cowley, W., Katona, L., Gouthas, G., Hough, L., Menpes, S., and Foss, C.: Depth to crystalline basement data package: South Australia, Geoscience Data Package, 3, 2018.

Daly, S.: Mineralization associated with the GRV and Hiltaba Suite granitoids: Earea Dam Goldfield, Glenloth Goldfield, Tarcoola Goldfield, The geology of South Australia, The Precambrian',(ed. Drexel, JF et al.), 1, 138–139, 1993.

Daly, S., Horn, C., and Fradd, W.: Tarcoola goldfield, Geology of the Mineral Deposits of Australia and Papua New Guinea: Australasian Institute of Mining and Metallurgy: Monograph, 14, 1049–1053, 1990.

Dimmen, V., Rotevatn, A., Peacock, D. C., Nixon, C. W., and Nærland, K.: Quantifying structural controls on fluid flow: Insights from carbonate-hosted fault damage zones on the Maltese Islands, Journal of Structural Geology, 101, 43–57, 2017.

Eisenlohr, B., Groves, D., and Partington, G.: Crustal-scale shear zones and their significance to Archaean gold mineralization in Western Australia, Mineralium Deposita, 24, 1–8, 1989.

Epuh, E., Okolie, C., Daramola, O., Ogunlade, F., Oyatayo, F., Akinnusi, S., and Emmanuel, E.: An integrated lineament extraction from satellite imagery and gravity anomaly maps for groundwater exploration in the Gongola basin, Remote Sensing Applications: Society and Environment, p. 100346, 2020.

Fairclough, M., Schwarz, M., and Ferris, G.: Interpreted crystalline basement geology of the Gawler Craton, Adelaide, South Australian Geological Survey, Special Map, 1: 1000000 series, 2003.

Ferris, G. M., Schwarz, M. P., and Heithersay, P.: The geological framework, distribution and controls of Fe-oxide Cu-Au mineralisation in the Gawler Craton, South Australia. Part I–Geological and tectonic framework, Hydrothermal iron oxide copper-gold and related deposits: A global perspective, 2, 9–31, 2002.

Florinsky, I. V.: Chapter 14 - Lineaments and Faults, in: Digital Terrain Analysis in Soil Science and Geology (Second Edition), edited by Florinsky, I. V., pp. 353 – 376, Academic Press, second edition edn., https://doi.org/https://doi.org/10.1016/B978-0-12-804632-6.00014-6, 2016.

Foss, C., Gouthas, G., Wilson, T., Katona, L., and Heath, P.: PACE Copper Gawler Craton Airborne Geophysical Survey, Region 9A, Childara Enhanced geophysical imagery and magnetic source depth models, Adelaide, Report Book, 2019/00008, 2019.

Fraser, G. L., Skirrow, R. G., Schmidt-Mumm, A., and Holm, O.: Mesoproterozoic Gold in the Central Gawler Craton, South Australia: Geology, Alteration, Fluids, and Timing, Economic Geology, 102, 1511–1539, https://doi.org/10.2113/gsecongeo.102.8.1511, 2007.

Gallant, J. C. and Dowling, T. I.: A multiresolution index of valley bottom flatness for mapping depositional areas, Water resources research, 39, 2003.

545   Geomatics, P.: PCI Geomatica User Guide, 2005.

González-Álvarez, I., Krapf, C., Fox, D., Noble, R., Reid, N., Verrall, M., Foss, C., Ibrahimi, T., Dutch, R., Jagodzinski, L., Cole, D., Lau, I., Robertson, J., and Pinchand, T.: Geochemical dispersion processes in deep cover and neotectonics in Coompana, Nullarbor plain, South Australia, vol. Paper 98, p. 5, Australian Exploration Geoscience Congress, 2-6 September, Perth, Western Australia, https://2019.aegc.com.au/programdirectory/docs/98.pdf, 2019.

550   González-Álvarez, I., Krapf, C., Kelka, U., Martínez, C., Albrecht, T., Ibrahimi, T., Pawley, M., Irvine, J., Petts, A., Gum, J., and Klump, J.: Linking cover and basement rocks in the Central Gawler Craton, South Australia, Report Book 2020/00029, p. 82, 2020.

Grauch, V. and Hudson, M. R.: Guides to understanding the aeromagnetic expression of faults in sedimentary basins: Lessons learned from the central Rio Grande rift, New Mexico, Geosphere, 3, 596–623, 2007.

Gum, J.: Gold mineral systems of the Central Gawler Craton, MESA Journal, 91, 51–65, 2019.

555   Hall, J.: Geophysical lineaments and deep continental structure, Philosophical Transactions of the Royal Society of London. Series A, Mathematical and Physical Sciences, 317, 33–44, 1986.

Hand, M., Reid, A., and Jagodzinski, L.: Tectonic framework and evolution of the Gawler Craton, Southern Australia, Economic Geology, 102, 1377–1395, 2007.

Hashim, M., Ahmad, S., Johari, M. A. M., and Pour, A. B.: Automatic lineament extraction in a heavily vegetated region using Landsat 560   Enhanced Thematic Mapper (ETM+) imagery, Advances in Space Research, 51, 874–890, 2013.

Heath, P., Dhu, T., Reed, G., and Fairclough, M.: Geophysical modelling of the Gawler Province, SA–interpreting geophysics with geology, Exploration Geophysics, 40, 342–351, 2009.

Hibburt, J.: The geology of South Australia, Vol. 2, The Phanerozoic, vol. 54, chap. Mulgathing Trough, p. 78, 1995.

Hoatson, D., Direen, N., Whitaker, A., Lane, R., Daly, S., Schwarz, M., and Davies, M.: Geophysical interpretation of the Harris Greenstone 565   Belt, Gawler Craton, South Australia, 2002.

Holden, D. J., Archibald, N. J., Boschetti, F., and Jessell, M. W.: Inferring geological structures using wavelet-based multiscale edge analysis and forward models, Exploration geophysics, 31, 617–621, 2000.

Hornby, P., Boschetti, F., and Horowitz, F.: Analysis of potential field data in the wavelet domain, Geophysical Journal International, 137, 175–196, 1999.

570   Hou, B.: Palaeochannel studies related to the Harris Greenstone Belt, Gawler Craton, South Australia: architecture and evolution of the Kingoonya Palaeochannel System, Report Book, 2004/1, CRC LEME Open File Report 154, p. 40, 2004.

Hovgaard, J. and Grasty, R.: Reducing statistical noise in airborne gamma-ray data through spectral component analysis, in: Proceedings of exploration, vol. 97, pp. 753–764, 1997.

Huang, Q., Kamenetsky, V. S., McPhie, J., Ehrig, K., Meffre, S., Maas, R., Thompson, J., Kamenetsky, M., Chambefort, I., Apukhtina, O., 575   et al.: Neoproterozoic (ca. 820–830 Ma) mafic dykes at Olympic Dam, South Australia: links with the gairdner large igneous province, Precambrian Research, 271, 160–172, 2015.

Ilugbo, S. and Adebiyi, A.: Intersection of lineaments for groundwater prospect analysis using satellite remotely sensed and aeromagnetic dataset around Ibodi, Southwestern Nigeria, International Journal of Physical Sciences, 12, 329–353, 2017.

Katona, L.: Gridding of South Australian ground gravity data, using the Supervised Variable Density Method, 2017.

580    Katona, L., Hutchens, M., and Foss, C.: Geological Survey of South Australia: An overview of the Gawler Craton Airborne Survey–new data and products, Preview, 2019, 24–26, 2019.

Kelka, U. and Martinez, C.: Automated surface and subsurface lineament extraction in the Central Gawler Craton - Remote Sensing and Geophysical Analysis, https://doi.org/10.25919/3d9y-eh30, 2019.

Kelka, U. and Westerlund, S.: FracG. v1, https://bitbucket.csiro.au/projects/FRACG/repos/fracg/, 2021.

585    Kelka, U., Westerlund, S., and Peeters, L.: FracG – An automated framework for discontinuity network characterization, 2021.

Kositcin, N.: Geodynamic synthesis of the Gawler Craton and Curnamona Province, Geoscience Australia, Record, 2010/27, 2010.

Krapf, C. and Gonzalez-Alvarez, I.: It is rather flat out there. . . Regolith mapping depicting intricate landsca pe patterns and relationships to bedrock geology and structures under cover on the Nullarbor Plain, in: Coompana Drilling and Geochemistry Workshop 2018 extended abstracts, Report Book, vol. 19, pp. 12–17, 2018.

590    Krapf, C., Irvine, J., Cowley, W., and M, F.: Regolith Map of South Australia, 1:2 000 000 Series (1st edition), Geological Survey of South Australia, 2012.

Langenheim, V. and Hildenbrand, T.: Commerce geophysical lineament—Its source, geometry, and relation to the Reelfoot rift and New Madrid seismic zone, Geological Society of America Bulletin, 109, 580–595, 1997.

Masoud, A. and Koike, K.: Applicability of computer-aided comprehensive tool (LINDA: LINeament Detection and Analysis) and shaded
595    digital elevation model for characterizing and interpreting morphotectonic features from lineaments, Computers & Geosciences, 106, 89 – 100, https://doi.org/https://doi.org/10.1016/j.cageo.2017.06.006, 2017.

Mohammadpour, M., Bahroudi, A., and Abedi, M.: Automatic Lineament Extraction Method in Mineral Exploration Using CANNY Algorithm and Hough Transform, Geotectonics, 54, 366–382, 2020.

Motta, J., Betts, P., de Souza Filho, C., Thiel, S., Curtis, S., and Armit, R.: Proxies for basement structure and its implications for Mesopro-
600    terozoic metallogenic provinces in the Gawler Craton, Journal of Geophysical Research: Solid Earth, 124, 3088–3104, 2019.

Nelson, R.: The Mulgathing Trough. South Australia, Quarterly Geological Notes, 58, 5–8, 1976.

O'Driscoll, E.: Observations of the lineament-ore relation, Philosophical Transactions of the Royal Society of London. Series A, Mathematical and Physical Sciences, 317, 195–218, 1986.

Pandey, P. and Sharma, L.: Image Processing Techniques Applied to Satellite Data for Extracting Lineaments Using PCI Geomatica and
605    Their Morphotectonic Interpretation in the Parts of Northwestern Himalayan Frontal Thrust, Journal of the Indian Society of Remote Sensing, 47, 809–820, 2019.

Pawley, M. and Wilson, T.: Solid geology interpretation of the GCAS 9A area, South Australia's 4D Geodynamic and Metallogenic Evolution, 2019.

Pawley, M., Irvine, J., Melville, A., Krapf, C., Thiel, S., Gonzalez-Alvarez, I., Kelka, U., and Martinez, C.: Automated lineament analysis of
610    the Gairdner Dolerite dyke swarm of the Gawler Craton, (*in press*), 2021.

Raghavan, V., Wadatsumi, K., and Masumoto, S.: Automatic extraction of lineament information from satellite images using digital elevation data, Nonrenewable Resources, 2, 148–155, 1993.

Reid, A. and Dutch, R.: Lithostratigraphy, structure and metamorphic architecture of a reworked Paleoproterozoic continental rift in the western Gawler Craton, What lies beneath the western Gawler Craton? 13GA-EG1E Seismic and Magnetotelluric Workshop 2015, Report
615    Book 2015/00029, pp. 15–27, 2015.

Reid, A. J., Jagodzinski, E. A., Fraser, G. L., and Pawley, M. J.: SHRIMP U–Pb zircon age constraints on the tectonics of the Neoarchean to early Paleoproterozoic transition within the Mulgathing Complex, Gawler Craton, South Australia, Precambrian Research, 250, 27 – 49, https://doi.org/https://doi.org/10.1016/j.precamres.2014.05.013, 2014.

620 Reid, A. J., Jagodzinski, E. A., Wade, C. E., Payne, J. L., and Jourdan, F.: Recognition of c. 1780 Ma magmatism and metamorphism in the buried northeastern Gawler Craton: Correlations with events of the Aileron Province, Precambrian Research, 302, 198–220, 2017.

Sanderson, D. J., Peacock, D. C., Nixon, C. W., and Rotevatn, A.: Graph theory and the analysis of fracture networks, Journal of Structural Geology, 125, 155–165, 2019.

Scheiber, T., Fredin, O., Viola, G., Jarna, A., Gasser, D., and Łapińska-Viola, R.: Manual extraction of bedrock lineaments from high-resolution LiDAR data: methodological bias and human perception, GFF, 137, 362–372, 2015.

625 Schmidt, P. W. and Clark, D.: Magnetic characteristics of the Hiltaba Suite Granitoids and Volcanics: Late Devonian overprinting and related thermal history of the Gawler Craton, Australian Journal of Earth Sciences, 58, 361–374, 2011.

Sheard, M., Keeling, J., Lintern, M., Hou, B., McQueen, K., and Hill, S.: A guide for mineral exploration through the regolith of the central Gawler Craton, South Australia, CRC LEME, 2008.

Sheikhrahimi, A., Pour, A. B., Pradhan, B., and Zoheir, B.: Mapping hydrothermal alteration zones and lineaments associated with orogenic
630 gold mineralization using ASTER data: A case study from the Sanandaj-Sirjan Zone, Iran, Advances in Space Research, 63, 3315–3332, 2019.

Shrivakshan, G. and Chandrasekar, C.: A comparison of various edge detection techniques used in image processing, International Journal of Computer Science Issues (IJCSI), 9, 269, 2012.

Skirrow, R. G., Bastrakov, E. N., Barovich, K., Fraser, G. L., Creaser, R. A., Fanning, C. M., Raymond, O. L., and Davidson, G. J.: Timing
635 of Iron Oxide Cu-Au-(U) Hydrothermal Activity and Nd Isotope Constraints on Metal Sources in the Gawler Craton, South Australia, Economic Geology, 102, 1441–1470, https://doi.org/10.2113/gsecongeo.102.8.1441, 2007.

Southworth, C. S.: Central Appalachian Cross-Strike Structural Discontinuities and Lineaments Compiled on Side-Looking Airborne Radar Image Mosaics: ABSTRACT, AAPG Bulletin, 69, 1448–1448, https://doi.org/10.1306/94885458-1704-11D7-8645000102C1865D, 1985.

Swain, G., Hand, M., Teasdale, J., Rutherford, L., and Clark, C.: Age constraints on terrane-scale shear zones in the Gawler Craton, southern
640 Australia, Precambrian Research, 139, 164–180, 2005.

Vassilas, N., Perantonis, S., Charou, E., Tsenoglou, T., Stefouli, M., and Varoufakis, S.: Delineation of lineaments from satellite data based on efficient neural network and pattern recognition techniques, in: Proc. Second Hellenic Conference on AI, pp. 355–365, Citeseer, 2002.

Wang, J.: LINDA—a system for automated linear feature detection and analysis, Canadian Journal of Remote Sensing, 19, 009–021, 1993.

Wheeler, R. L.: Cross-strike structural discontinuities: possible exploration tool for natural gas in Appalachian overthrust belt, AAPG Bul-
645 letin, 64, 2166–2178, 1980.

Wilson, T., Pawley, M., and Verco, R.: Structural geology and GCAS: implications for gold systems in the central Gawler Craton, in: Geological Survey of South Australia Discovery Day 2018: presentation abstracts and posters, edited by A.R., R., vol. Report Book, 2018/00034, pp. 9–14, Government of South Australia. Department for Energy and Mining, 2018.

Witt, W., Hickman, A., Townsend, D., and Preston, W.: Mineral Potential of the Archaean Pilbara and Yilgarn Cratons, Western Australia,
650 AGSO Journal of Australian Geology and Geophysics, 17, 201–222, 1998.

Xu, J., Wen, X., Zhang, H., Luo, D., Li, J., Xu, L., and Yu, M.: Automatic extraction of lineaments based on wavelet edge detection and aided tracking by hillshade, Advances in Space Research, 65, 506–517, 2020.

Zhang, L., Wu, J., Hao, T., and Wang, J.: Automatic lineament extraction from potential-field images using the Radon transform and gradient calculation, Geophysics, 71, J31–J40, 2006.